ADVANCES IN MATERIALS SCIENCE, Vol. 25, No. 1 (83), March 2025

DOI: 10.2478/adms-2025-0004

Abid Hussain[1]*, Afzal Khan[1], Muhammad Imran Khan[2], Saif Ur Rehman[3]

[1]*Department of Mechanical Engineering, University of Engineering and Technology Peshawar, Pakistan*
[2]*Ghulam Ishaq Khan (GIK) Institute of Engineering and Science and Technology, Topi District Swabi, Khyber Pakhtunkhwa, Pakistan*
[3]*Institute of Industrial Control System, Rawalpindi, Pakistan*

[*]*abidhussain@uetpeshawar.edu.pk*

ENHANCING MICROSTRUCTURAL AND THERMAL PROPERTIES OF TiNiPd SHAPE MEMORY ALLOYS THROUGH COPPER ADDITION

ABSTRACT

This study explores how the addition of copper (Cu) addition impacts the microstructural and thermal properties of shape memory alloys (SMAs), specifically TiNiPd alloys. Two compositions, 0Cu and 10Cu, were analyzed using X-ray diffraction (XRD), scanning electron microscopy (SEM), Optical Microscopy (OM) and differential scanning calorimetry (DSC). SEM revealed second-phase precipitates distributed along grain boundaries in both alloys, with sizes ranging from 0.9 to 2.9 μm; however, Cu addition reduced precipitate density without affecting size. The grain size increased significantly from 12.5 μm in 0Cu to 17.5 μm in 10Cu, attributed to decreased nickel content and reduced pinning effects of precipitates. Aging at 600°C and 700°C further influenced precipitate behavior and transformation temperatures, with Cu-containing alloys demonstrating enhanced thermal characteristics. DSC analysis indicated significant increases in transformation temperatures and decreased thermal hysteresis with Cu addition. These results highlight the promise of Cu as a viable substitute for Ni in enhancing the properties of TiNiPd SMAs.

Keywords: *TiNiPd SMAs; heat treatment; SEM; XRD; DSC*

INTRODUCTION

SMAs are an important class of materials known for their ability to undergo significant deformation and revert to their original shape upon heating [1]. This unique property is primarily due to reversible phase transformations, specifically the transition between austenite and martensite phases [2]. Among the various SMAs, TiNi-based alloys are widely studied due to their excellent mechanical properties, biocompatibility, and shape memory effect making them

Received:24.10.2024; Received in revised form: 5.01.2025 ; Accepted: 6.01.2025

suitable for a range of applications including actuators, sensors, and biomedical devices [3]. The performance of TiNi alloys can be significantly influenced by the addition of alloying elements. Nickel (Ni) is a principal constituent of these alloys, but its substitution with other elements, such as Cu, can tailor the material's properties [4]. Cu is of particular interest because it can alter the phase transformation temperatures, improve the alloy's ductility, and influence microstructural characteristics such as grain size and precipitate formation [5].

The addition of Cu to TiNiPd alloys significantly influences the phase transformation behavior and thermal stability [6]. Cu has been observed to modify the martensitic transformation temperatures, making it possible to tailor the operating range of the alloy for specific applications [7]. By adjusting the concentration of Cu, it is possible to shift the transformation temperatures to more desirable levels, thereby expanding the usability of TiNiPd alloys in practical scenarios, particularly in environments where conventional operating conditions are unsuitable. Furthermore, Cu addition plays a crucial role in enhancing the microstructural properties of TiNiPd alloys [8].

The presence of Cu can facilitate the formation of more refined microstructures, leading to improved grain boundary characteristics and enhanced dislocation mobility. These microstructural changes are vital for improving the mechanical properties, such as ductility and toughness, which are critical for applications that involve cyclic loading or dynamic stress conditions [9]. Thermal properties are another area where Cu addition can have a profound impact. Enhanced thermal conductivity resulting from Cu incorporation can lead to more efficient thermal activation of the shape memory effect [10]. This is particularly relevant in applications such as actuators and sensors, where rapid thermal response is essential for effective operation [11]. Previous studies have shown that the microstructural evolution in SMAs is closely linked to the presence of second-phase precipitates, which can serve as nucleation sites and affect grain growth [12]. The size, shape, and distribution of these precipitates play a crucial role in defining the mechanical and thermal behavior of the alloys [13]. For instance, smaller and denser precipitates may enhance strength through a mechanism known as pinning, while larger or less dense precipitates may lead to increased ductility [14]. The improvement of mechanical and shape memory characteristics in the $Ti_{50.6}Ni_{49.4}$ SMA. This enhancement was achieved by homogenizing the Ti_2Ni precipitates formed during selective laser melting (SLM) through a subsequent heat treatment. We thoroughly examined the microstructural changes, transformation behaviors, and the resulting mechanical and shape memory properties [15]. A titanium-rich Ti–Ni–Cu ternary SMA with a mixed atomic composition of Ti–44at. %Ni–3at. %Cu, utilizing a near-equiatomic commercial TiNi binary SMA substrate. This work demonstrates the potential of the elemental powder direct energy deposition (DED) process to effectively bond distinct SMA types and create alloys exhibiting diverse shape memory behaviors [16]. Employing Selective Laser Melting (SLM) and Electron Beam Melting (EBM) allows for precise control over microstructural development, facilitating the production of intricate, multifunctional alloys. These techniques contribute to enhanced electrical properties, biocompatibility, strength, fatigue resistance, and recovery performance [17]. Rolling of TiNiCu SMAs at room temperature followed by annealing produced a finer grain size than rolling at 0°C or cryogenic temperatures. The variation in matrix composition after annealing, influenced by the initial rolling temperature, underscores the impact of stored energy on the redistribution of elements [18]. The functional properties of a (Ni,Cu)-rich $Ti_{49}Ni_{41}Cu_{10}$ shape memory alloy subjected to a 168-hour aging treatment at 400°C. The aging process led to an increase in Vickers hardness, attributed to the

formation of densely distributed nano-scale C11b $Ti(Ni,Cu)_2$ precipitates. These precipitates demonstrated a coherent interface with the matrix and had an approximate thickness of 2 nm [19]. The stress-strain behavior of nanocrystalline/amorphous NiTi samples exhibits a distinctive form of pseudoelasticity, lacking a stress plateau and hysteresis. This unique response is strongly influenced by a high density of lattice defects, dislocations, and the nanoscale grain size, which play crucial roles in the mechanisms of martensitic transformation and phase changes [20].

In this study, we focus on the effects of replacing Ni with 10% Cu in TiNiPd alloys, specifically examining the resulting microstructural features and their correlation with phase transformation behavior. We employ various analytical techniques, including SEM, OM, energy-dispersive X-ray spectroscopy (EDS), DSC, and XRD to comprehensively characterize the SMAs. Initial analyses reveal that while the addition of Cu does not significantly alter the size of precipitates, it leads to a marked decrease in their density. This reduction in precipitate density is expected to impact the grain growth behavior, potentially resulting in larger grain sizes in Cu-containing alloys compared to those with pure Ni. Furthermore, the influence of aging temperature on precipitate formation and phase stability is investigated to understand how heat treatment affects the transformation characteristics of the SMAs. Through this research, we aim to elucidate the relationship between alloy composition, microstructural evolution, and thermal properties, thereby providing insights into the design and optimization of TiNiPd SMAs for advanced applications. Our findings contribute to the broader understanding of how specific alloying strategies can enhance the performance of SMAs, opening avenues for future investigations into novel alloy systems.

MATERIALS AND METHODS

The SMAs used in this study were based on the TiNiPdCu system, specifically designed with two compositions: 0Cu (baseline alloy with no copper addition) and 10Cu (alloy with 10% copper replacing nickel). The alloys were synthesized using high-purity elemental titanium (Ti), nickel (Ni), palladium (Pd), and copper (Cu). The stoichiometric amounts of each element were carefully calculated based on the desired alloy composition. The elements were individually weighed using precision balances to ensure accurate proportions, as even minor deviations could affect the alloy's characteristics. The weighed elements were placed into a vacuum arc furnace. This equipment was chosen for its ability to provide a controlled, high-temperature environment, minimizing contamination and ensuring thorough melting. The furnace was evacuated to remove air and other gases, creating a vacuum environment. This step was critical to prevent oxidation or unwanted reactions during melting. The elements were subjected to high-temperature arc melting. An electric arc was used as the heat source to melt the metals. To ensure homogeneity, the melting process was repeated multiple times. The alloy was remelted and flipped between each cycle to guarantee uniform mixing of all constituent elements. After achieving a homogeneous melt, the alloy was allowed to cool and solidify under controlled conditions. This step was important to stabilize the microstructure and prevent the formation of unwanted phases. The synthesized alloys were carefully extracted from the furnace and stored in an inert or controlled environment to prevent contamination or oxidation before further processing or characterization. Following melting, the alloys were subjected to solution treatment at 900°C for 2 hours, followed by water quenching to preserve the high-temperature phase. The samples were then sectioned into smaller pieces for subsequent analysis. For aging studies, the samples were aged at two

different temperatures: 600°C and 700°C for 1 hour. After aging, the samples were air-cooled to room temperature. The schematic diagram is shown in Figure 1.

The microstructural analysis was performed using a SEM equipped with energy-dispersive X-ray spectroscopy (EDS) for compositional analysis. Samples were prepared by polishing and then etched to reveal grain boundaries. SEM images were captured at various magnifications to observe the morphology and distribution of second-phase precipitates. The samples were further examined using an optical microscope at magnifications of 500X and 800X to assess grain structure and phase distribution. XRD analysis was conducted using a powder X-ray diffractometer with Cu Kα radiation (λ = 1.5406 Å). The scans were performed over a 2θ range of 20° to 80° to identify phase content and assess the lattice parameters. The resulting diffraction patterns were analyzed for peak positions and intensities corresponding to the B19 martensite phase and any secondary phases. DSC measurements were carried out to evaluate the phase transformation temperatures of the SMAs. The samples were subjected to heating and cooling cycles at a controlled rate of 10 °C/min. The transformation temperatures, including the Ms and Af, were determined from the DSC curves, which were plotted to analyze the thermal behavior.

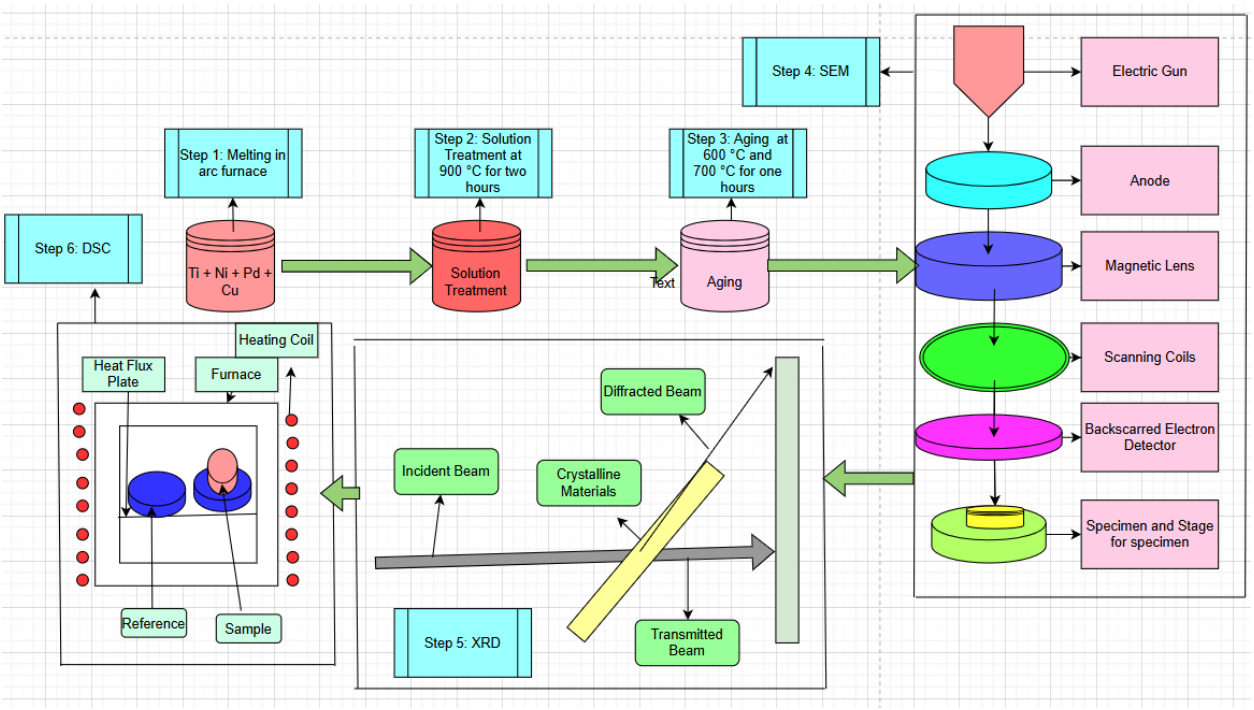

Fig. 1. Schematic diagram of the heat treatment and characterization of SMAs

The data collected from SEM, XRD, and DSC analyses were interpreted to establish relationships between microstructural characteristics, phase behavior, and transformation temperatures in the SMAs. Statistical methods were employed where appropriate to ensure the reliability of the results. Figure 2 (a-c) presents the images of SEM, XRD and DSC respectively for visual support.

Fig. 2. Images of (a) SEM, (b) XRD and (c) DSC

RESULTS AND DISCUSSION

SEM of 0Cu and 10Cu solution treated SMAs

The SEM images of the 0Cu and 10Cu solution-treated SMAs are shown in Figure 3. It is evident from these images that both SMAs contain second-phase precipitates with low-density, which appear black and are randomly spread along the boundaries of the grain. The average size of these precipitates ranges from 0.9 to 2.9 μm, and they predominantly exhibit circular or elliptical shapes. In the previous study the average size of these precipitates were found to be 0.6 to 1.2 μm [21].

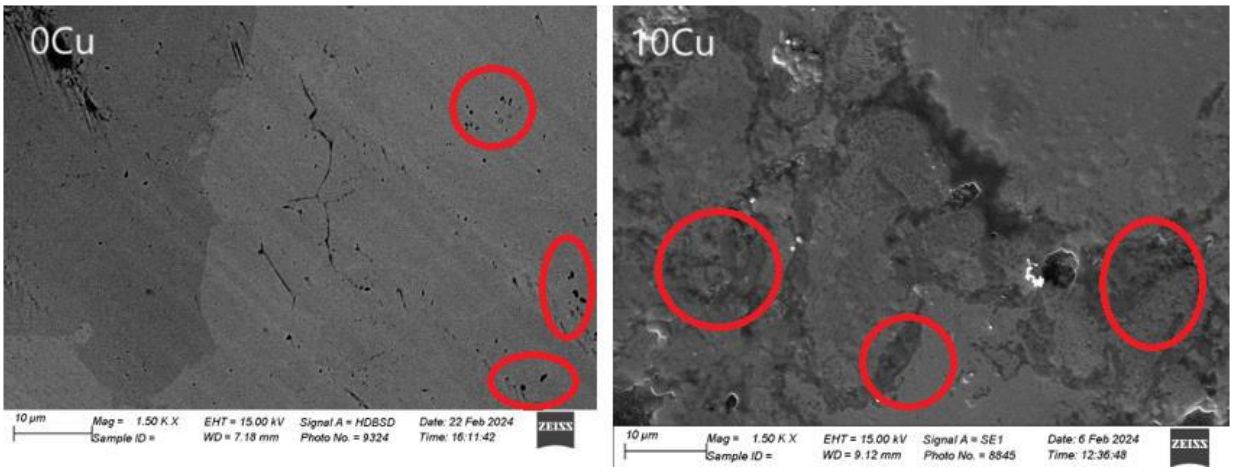

Fig. 3. Second phase precipitates found in 0Cu and 10 Cu SMAs

This suggests that the addition of Cu does not influence the size of the precipitates; however, an increase in Cu content correlates with a reduction in their density. EDS analysis was conducted to determine the chemical composition of the material and the second-phase precipitates, with the resulting pattern presented in Figure 4.

Optical Microscopy of 0Cu and 10Cu solution treated SMAs

The optical micrographs of the 0Cu and 10Cu SMAs at magnifications of 500X and 800X, respectively, in their solution-treated state are shown in Figures 5 and 6 respectively. These images show that both SMAs feature a single-phase structure typical of twinned martensite, with well-defined grain boundaries. Grain size was evaluated using the intercept method, which entails drawing several straight lines of uniform length across the micrographs to analyze the grain structure. The grains intersected by each line were counted, and the total line length was divided by the average number of intersected grains across all lines. The average grain diameter was then calculated by dividing this figure by the linear magnification of the images. The average grain sizes for the 0Cu and 10Cu SMAs were calculated to be 12.5 μm and 17.5 μm, respectively. These findings indicate that substituting Cu for Ni led to an increase in grain size. Specifically, the grain size of the 0Cu SMA (12.5 μm) increased by approximately 40% to 17.5 μm in the 10Cu SMA. This increase can be linked to the reduced nickel content, which also resulted in a decrease in the formation of second-phase precipitates.

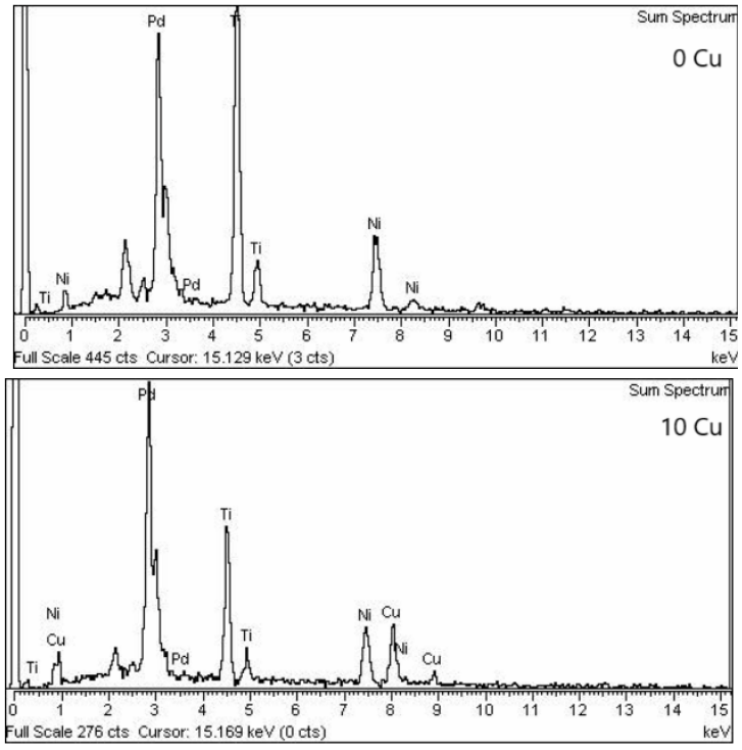

Fig. 4. EDS spectrum for 0 Cu and 10 Cu solution treated SMAs

As the Cu content rose from 0% to 10%, the reduction in these precipitates allowed for greater grain growth. In the case of the 10Cu SMA, the lower density of precipitates resulted in less pinning effect, facilitating more significant grain growth compared to the 0Cu SMA.

Consequently, the increase in Cu content led to an enhanced grain size due to diminished pinning effects from second-phase precipitates.

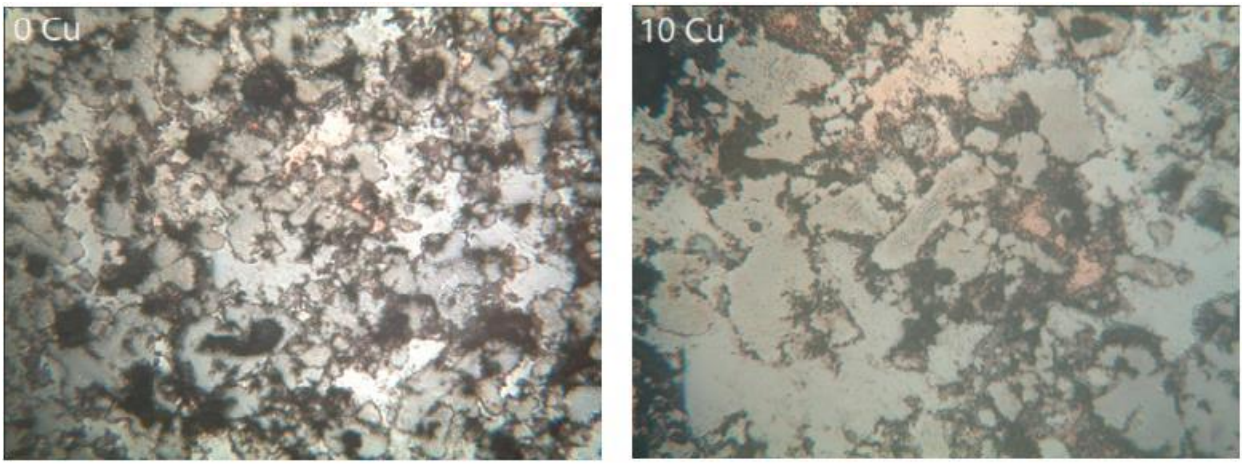

Fig. 5. Optical Microscopy of 0Cu and 10 Cu SMAs at 500X

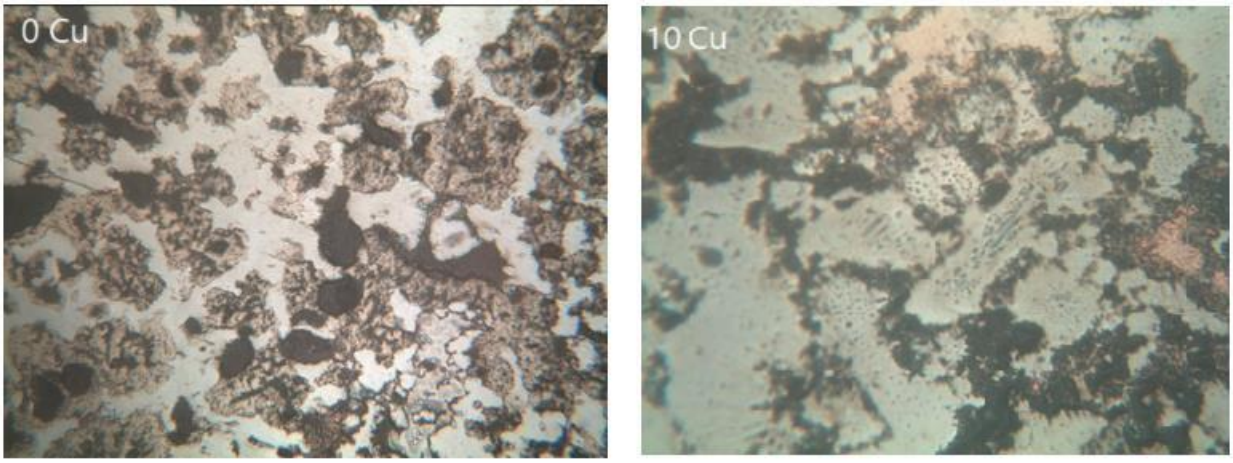

Fig. 6. Optical Microscopy of 0Cu and 10 Cu SMAs at 800X

SEM of 0Cu and 10Cu aged SMAs

To examine how different aging temperatures affect both SMAs, SEM analysis was conducted. Figure 7 displays SEM images of the 0Cu SMA after aging at 600°C and 700°C. These images indicate that only the second-phase precipitates formed during the solidification process were present. Notably, there were no signs of precipitation along the grain boundaries or within the grains as a result of aging.

The precipitation behavior of the 10Cu SMA under the same aging conditions are illustrated in Figure 8. Figure 8a shows the microstructure of the SMA after aging at 600°C, where heterogeneous precipitates were observed on both the grain boundaries and within the grain interiors. The precipitates in this image exhibited thread-like structures of varying lengths. Figure 8b depicts the microstructure of the SMA after aging at 700°C, revealing the presence of fewer, larger precipitates. At 700°C the behavior of precipitates was distinctly different from that

observed at 600°C. Additionally, the formation of nano-sized precipitates during annealing at different temperatures from 550°C-650°C for one hour after a 40% cold deformation was reported by Khan et al. [22].

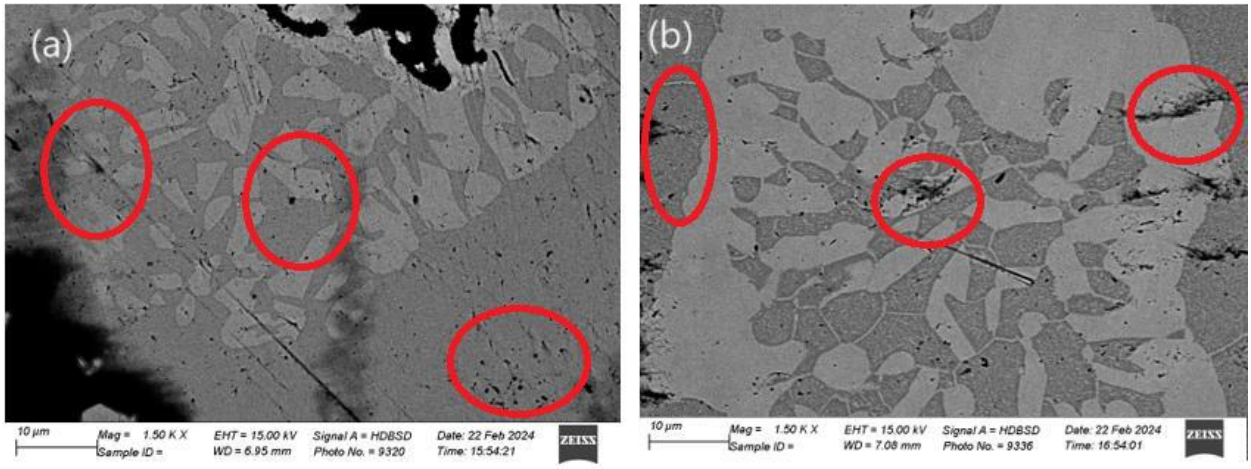

Fig. 7. SEM images of 0 Cu SMA aged at (a) 600°C and (b) 700°C

However, nano-scale precipitates were observed in that study and displayed different morphologies, such as rod-like shapes and elliptical as compare to the current investigation. Furthermore, the precipitation mechanisms in annealing were found to differ significantly from those during the aging heat treatment process. While cold deformation after annealing creates sites of heterogeneous nucleation due to problems produced due to deformation [23], the age-hardening process depends on grain boundaries of high energy to serve as sites of nucleation for precipitation.

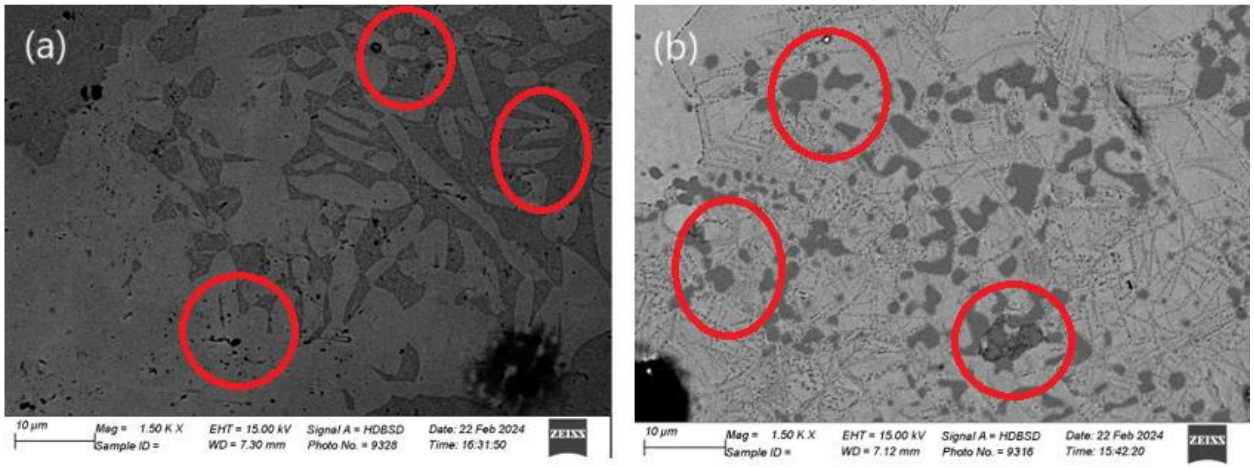

Fig. 8. SEM images of 10 Cu SMA aged at (a) 600°C and (b) 700°C

XRD of 0Cu and 10Cu solution treated SMAs

Phase analysis was conducted using an X-Ray Diffractometer with Cu Kα (λ = 1.5406 Å) radiation. as shown in Figure 9. The XRD profiles were obtained in a 2θ range of 20 to 80 degrees at room temperature in the martensite phase. The analysis revealed that the prominent peaks were mainly located between diffraction angles of 30 and 60 degrees; thus, the XRD

profiles are displayed within this range. Figure 9 illustrates the XRD pattern of solution-treated TiNiPdCu SMAs with adding content of Cu. All peaks in the XRD pattern indicate the presence of only the orthorhombic martensite phase (B19), confirming that the alloys consist solely of this phase at ambient temperature. The second phase precipitates, specifically Ti_2Pd (black precipitate) in the 0Cu SMA and TiNiPd (white precipitate) in the 10Cu SMA, were not detected in the XRD analysis, although they were visible in the SEM presented in Figure 3. This absence of peaks for Ti_2Pd in the 0Cu SMA and TiNiPd in the 10Cu SMA may be attributed to their low volume fraction. Upon adding Cu to the TiNiPd SMAs, a steady shift of the B19 martensite peaks towards smaller angles of 2θ was detected. Notably, the strongest martensite peak of B19 (111) at approximately 43 degrees for the 0Cu alloy shifted to a lower angle in the 10Cu SMA. This decrease in the diffraction angle with increased Cu content is likely due to an increase in lattice constants, attributed to the greater atomic radius of Cu as compared to that of Ni.

XRD of 0Cu SMAs aged at 600°C and 700°C

The XRD pattern at ambient temperature for the aging of 0Cu SMAs at a temperature of 600°C and 700°C are presented in Figure 10. Four peaks, (002), (020), (111), and (022), represent the B19 martensite phase, confirming that the predominant phase at room temperature remains B19 martensite. The stoichiometric TiNiPd SMAs did not exhibit any phase changes upon aging at 600°C and 700°C.

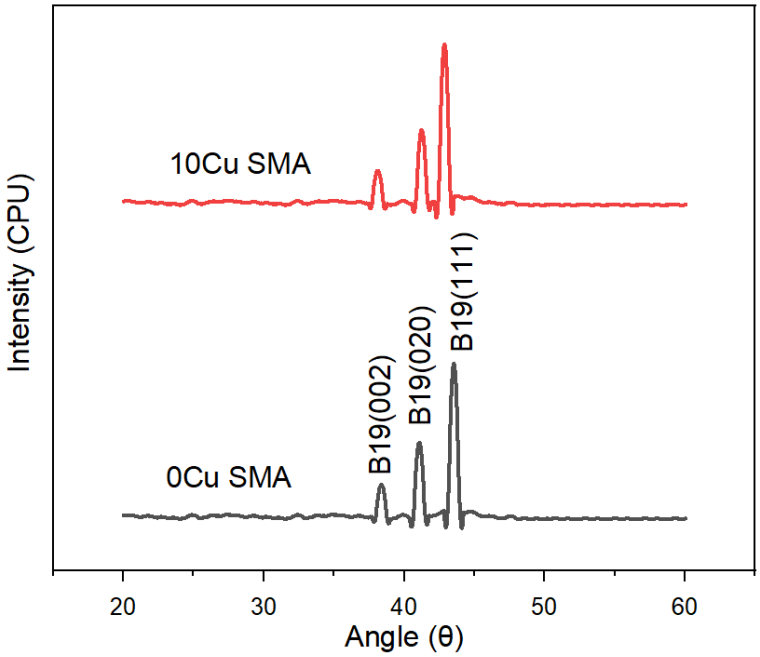

Fig. 9. XRD profile for solution treated 0 Cu and 10 Cu SMAs

XRD of 10Cu SMAs solution treated and aged at 600°C and 700°C

The XRD patterns at ambient temperature for the solution-treated and aging of 10Cu SMAs at 600°C and 700°C are shown in Figure 11. The XRD pattern for the solution-treated sample reveals four peaks, (002), (020), (111), and (022), all corresponding to the B19 martensite phase. Aging the alloy at 600 °C resulted in peaks related to newly formed second-phase precipitates

showing maximum intensity, indicating a higher volume fraction of these precipitates. Based on the XRD profile and reference [24], the peaks adjacent to the (111) reflection were identified as Ti_2Pd and TiPdCu, respectively. The precipitation behavior observed aligns well with the microstructures shown in Figure 8 (a–b). When the temperature of aged SMAs was increased to 700°C, the XRD profile changed significantly, with peaks related to Ti_2Pd and TiPdCu disappearing. While Figure 8b indicated the presence of both types of precipitates, low-density precipitates at 700°C, they were not detectable in the XRD pattern, likely due to their small volume fraction. The XRD patterns for the SMAs after aging at a temperature of 700°C were consistent with those of the solution-treated SMA, confirming that all peaks corresponded to the orthorhombic martensite phase (B19).

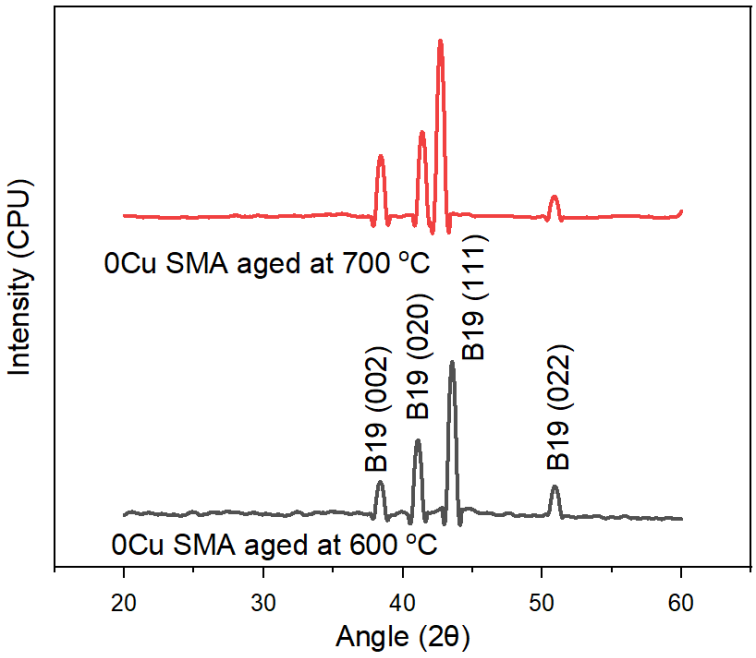

Fig. 10. XRD profile for 0 Cu SMA aged at 600°C and 700°C

DSC of 0Cu and 10Cu solution treated SMAs

The DSC cooling and heating cycles for the 0 Cu and 10 Cu SMAs, which were solution-treated at a temperature of 900°C for 2 hours are presented in Figure 12. The phase transformation temperatures obtained from these DSC cycles are plotted again in Figure 13 to illustrate the changes in transformation temperatures when 10% Cu replaces Ni in comparison to the baseline 0Cu SMA. Both SMAs displayed similar behavior, characterized by a single-stage martensite transformation, with clearly-defined peaks and accurately determined transformation temperatures. Notably, the of heat transformation (ΔHc), which represents the area under the cooling curve during the forward transformation cycle, as well as the transformation heat (ΔHh) during the reverse transformation cycle (area under the heating curve), increased with the addition of Cu. Specifically, the martensite start temperature (Ms) for the 0Cu alloy rose by 27°C, increasing from 141°C to 168°C, while the austenite finish temperature (Af) increased by 24°C, from 165°C to 189°C, with the substitution of Cu (at. 10%) for Ni. Additionally, it is noteworthy

that the thermal hysteresis remained consistent. These experimental results indicate that replacing Ni with Cu (at. 10%) significantly raises the transformation temperatures, while the thermal hysteresis remains unchanged.

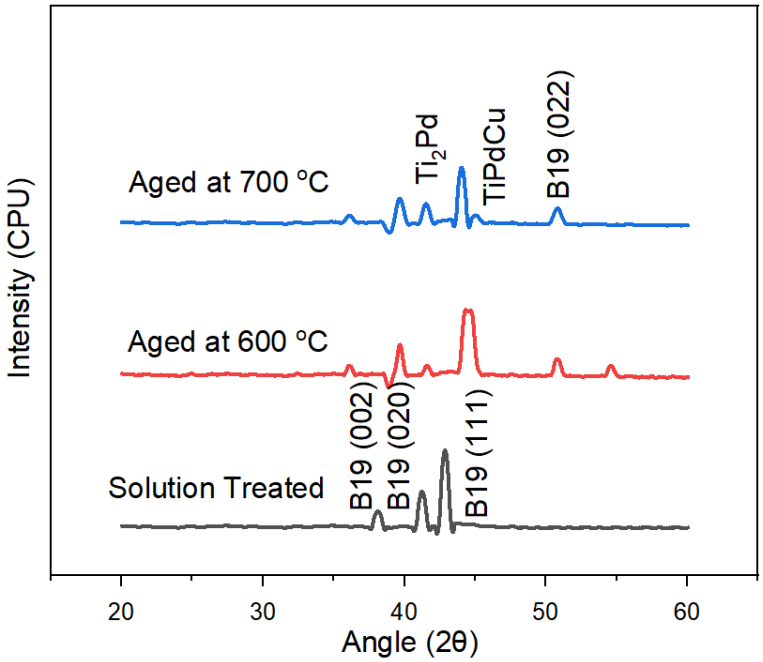

Fig. 11. XRD profile for 10 Cu SMA solution treated and aged at 600°C and 700°C

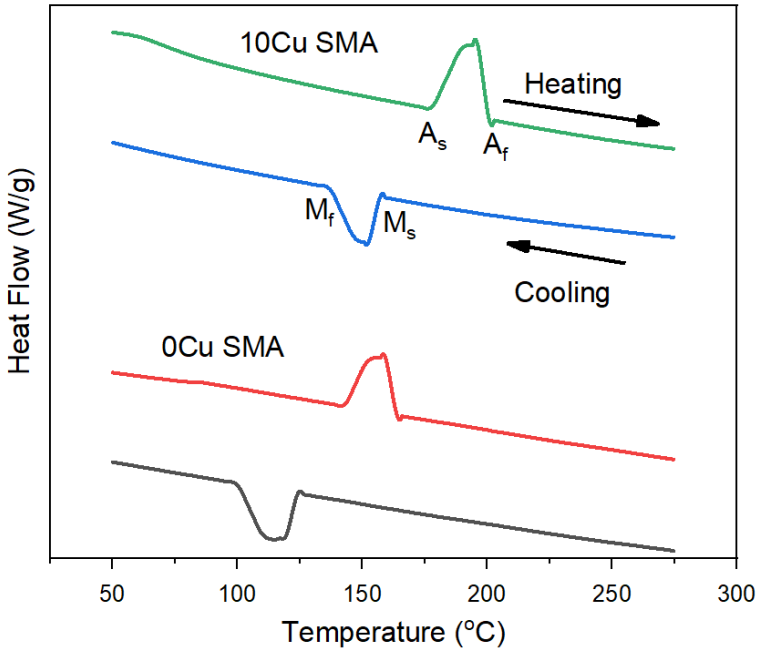

Fig. 12. DSC heating and cooling cycles of 0Cu and 10Cu solution treated SMAs

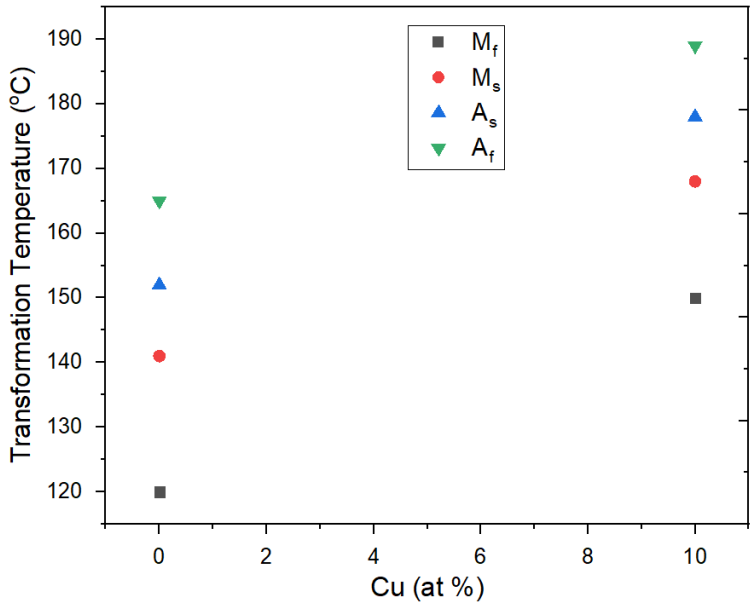

Fig. 13. Effect of Cu-contents on transformation temperatures

DSC of 10Cu SMAs solution treated and aged at 600°C and 700°C

The DSC cooling and heating cycles for the 0Cu SMA that was solution-treated and aged at a temperature of 600°C and 700°C are presented in Figure 14. Figure 15 depicts the changes in transformation temperatures corresponding to the increase in aging temperatures. The DSC cycles for the SMAs aged at both 600°C and 700°C exhibited well-defined peaks, with a noticeable increase in peak sharpness as the temperature of aging rose from 600°C to 700°C.

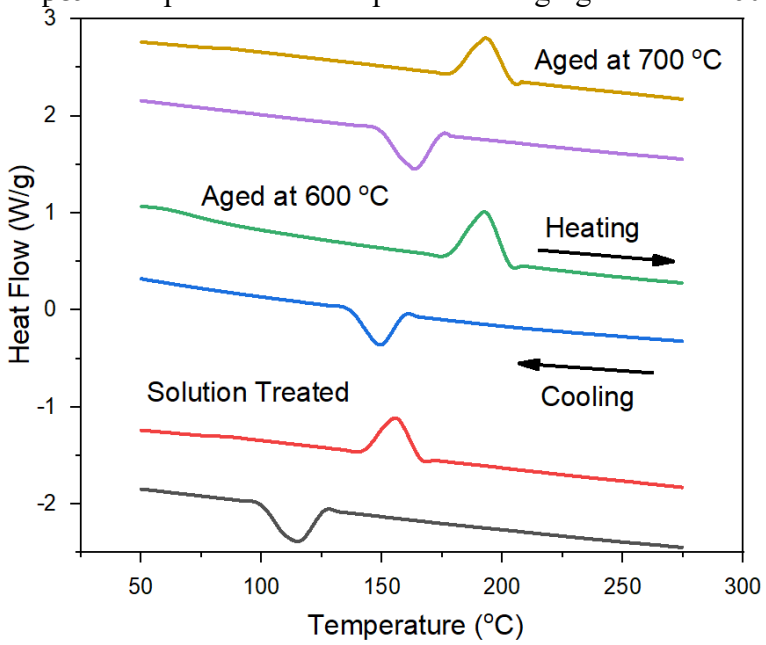

Fig. 14. DSC cooling and heating cycles of the solution treated SMA of 0Cu

Consequently, the transformation heats released during the forward transformation and absorbed during the reverse transformation increased with higher aging temperatures. For the

600°C-aged SMA, the Ms rose by 8°C, from 141°C to 149°C, while the Af increased by 9°C, from 168°C to 177°C, as the temperature of aging increased to 700 °C. Additionally, a slight increase in thermal hysteresis of the 0Cu alloy was noted with rising aging temperatures. The observed increase in transformation temperatures for the 0Cu SMA due to higher aging temperatures can be attributed solely to grain growth, as no precipitation was detected during the aging of the 0Cu SMA. As the aging temperature changed from 600°C to 700°C, the peaks of transformation in the DSC cycles resulted in a well-developed profile with appropriate heights.

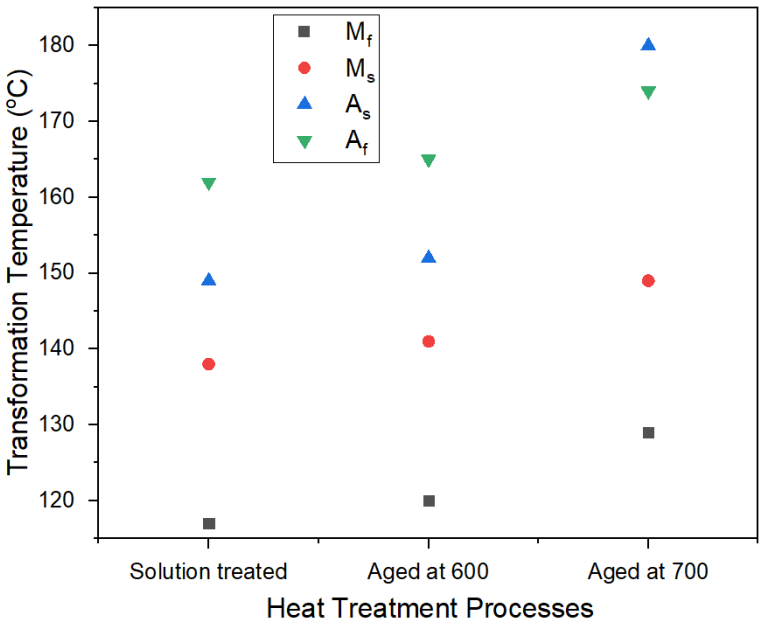

Fig. 15. Effect of heat treatment on transformation temperatures

CONCLUSIONS

The findings of this study demonstrate that replacing 10% Cu for Ni in TiNiPd SMAs significantly enhances the SMAs' thermal and microstructural properties. The addition of Cu resulted in a marked increase in average grain size and a reduction in the density of second-phase precipitates, suggesting that Cu may play a critical role in optimizing grain growth mechanisms. Furthermore, the aging treatment revealed that higher temperatures promoted the formation of additional precipitates, which correlated with increases in transformation temperatures and the sharpness of thermal peaks in DSC analysis. The increased transformation temperatures and reduced thermal hysteresis in the Cu-containing alloy indicate improved performance characteristics, making these materials more suitable for applications requiring precise shape memory effects. The main finding of current research is given below.

- SEM: Second-phase precipitates (0.9–2.9 μm, circular/elliptical) with low density appear black and are randomly distributed along grain boundaries.

- OM: Average grain sizes are 12.5 μm (0Cu) and 17.5 μm (10Cu), showing a 40% increase in grain size with Cu substitution for Ni.
- XRD (solution-treated): Four peaks ((002), (020), (111), (022)) correspond to the B19 martensite phase.
- Aging at 600°C: Higher volume fraction of second-phase precipitates observed..
- XRD (aged at 700°C): Peaks consistent with the solution-treated SMA, confirming the orthorhombic martensite phase (B19).
- Replacing Ni with 10 at.% Cu increases transformation temperatures without affecting thermal hysteresis..
- As Aging temperature shift from 600°C to 700°C improves DSC peak profiles with better-defined heights.

Overall, this study confirms that Cu is a promising candidate for enhancing the properties of TiNiPd SMAs, paving the way for future research into alloy optimization and application development.

Conflicts of interests

The authors declare that there is no conflict of interests.

REFERENCES

1. İ. Özkul, M. A. Kurgun, E. Kalay, C. A. Canbay, and K. Aldaş, "Shape memory alloys phenomena: classification of the shape memory alloys production techniques and application fields," Eur. Phys. J. Plus, vol. 134, no. 12, p. 585, 2019.
2. K. Tanaka, S. Kobayashi, and Y. Sato, "Thermomechanics of transformation pseudoelasticity and shape memory effect in alloys," Int. J. Plast., vol. 2, no. 1, pp. 59–72, 1986.
3. V. Pushin, N. Kuranova, E. Marchenkova, and A. Pushin, "Design and development of Ti–Ni, Ni–Mn–Ga and Cu–Al–Ni-based alloys with high and low temperature shape memory effects," Materials, vol. 12, no. 16, p. 2616, 2019.
4. C. Velmurugan, V. Senthilkumar, S. Dinesh, and D. Arulkirubakaran, "Machining of NiTi-shape memory alloys-A review," Mach. Sci. Technol., vol. 22, no. 3, pp. 355–401, May 2018, doi: 10.1080/10910344.2017.1365894.
5. M. Kaftaranova, V. Hodorenko, S. Anikeev, N. Artyukhova, A. V. Shabalina, and V. Gunther, "Investigation of the effect of copper addition on physical and mechanical properties of TiNi-Cu porous alloy," Metals, vol. 12, no. 10, p. 1696, 2022.
6. S. U. Rehman et al., "Influence of Cu addition on transformation temperatures and thermal stability of TiNiPd high temperature shape memory alloys," Proc. Inst. Mech. Eng. Part J. Mater. Des. Appl., vol. 233, no. 5, pp. 800–808, May 2019, doi: 10.1177/1464420717702679.
7. M. Khan, H. Y. Kim, T. Nam, and S. Miyazaki, "Effect of Cu addition on the high temperature shape memory properties of Ti50Ni25Pd25 alloy," J. Alloys Compd., vol. 577, pp. S383–S387, 2013.

8. M. I. Khan, H. Y. Kim, and S. Miyazaki, “A Review of TiNiPdCu Alloy System for High Temperature Shape Memory Applications,” Shape Mem. Superelasticity, vol. 1, no. 2, pp. 85–106, 2015, doi: 10.1007/s40830-015-0019-y.
9. M. I. Khan, H. Y. Kim, Y. Namigata, T. Nam, and S. Miyazaki, “Combined effects of work hardening and precipitation strengthening on the cyclic stability of TiNiPdCu-based high-temperature shape memory alloys,” Acta Mater., vol. 61, no. 13, pp. 4797–4810, 2013.
10. S. ur Rehman, M. Khan, A. N. Khan, L. Ali, S. I. H. Jaffery, and M. Khurram, “Quaternary alloying of copper with Ti50Ni25Pd25 high temperature shape memory alloys,” Mater. Sci. Eng. A, vol. 763, p. 138148, 2019.
11. R. Radhamani and M. Balakrishnan, “The effect of copper on phase transformation, microstructure and mechanical characterization of Ni50-x Ti50 Cux shape-memory alloy,” Proc. Inst. Mech. Eng. Part J. Mater. Des. Appl., vol. 237, no. 5, pp. 1137–1145, 2023, doi: 10.1177/14644207221137257.
12. D. Kim, C. Park, J. Lee, K. Hong, Y. Park, and W. Lee, “Microstructure, shape memory behavior and mechanical properties of hot rolled Fe-17Mn-5Si-5Cr-4Ni-0.3 C-1Ti shape memory alloy,” Eng. Struct., vol. 239, p. 112300, 2021.
13. J. Bhagyaraj, K. V. Ramaiah, C. N. Saikrishna, and S. K. Bhaumik, “Behavior and effect of Ti2Ni phase during processing of NiTi shape memory alloy wire from cast ingot,” J. Alloys Compd., vol. 581, pp. 344–351, 2013.
14. G. Tadayyon et al., “Effect of different stages of deformation on the microstructure evolution of Ti-rich NiTi shape memory alloy,” Mater. Charact., vol. 125, pp. 51–66, 2017.
15. H. Z. Lu et al., “Simultaneous enhancement of mechanical and shape memory properties by heat-treatment homogenization of Ti2Ni precipitates in TiNi shape memory alloy fabricated by selective laser melting,” J. Mater. Sci. Technol., vol. 101, pp. 205–216, 2022.
16. Y. Chen, C. Ortiz Rios, B. McLain, J. W. Newkirk, and F. Liou, “TiNi-based Bi-metallic shape-memory alloy by laser-directed energy deposition,” Materials, vol. 15, no. 11, p. 3945, 2022.
17. S. Ahmad et al., “Innovations in Additive Manufacturing of Shape Memory Alloys: Alloys, Microstructures, Treatments, Applications,” J. Mater. Res. Technol., vol. 32, pp. 4136-4197, 2024, https://www.sciencedirect.com/science/article/pii/S2238785424020052
18. S. M. R. Varukuti, K. N. Chaithanya Kumar, and K. S. Suresh, “Effect of rolling temperature and annealing on grain refinement in TiNiCu shape memory alloys,” J. Mater. Eng. Perform., pp. 1–13, 2023.
19. Y.-T. Hsu, C.-T. Wu, and C.-H. Chen, “Nanoscale-precipitate-strengthened (Ni, Cu)-rich TiNiCu shape memory alloy with stable superelasticity and elastocaloric performance,” J. Alloys Compd., vol. 997, p. 174937, 2024.
20. M. Ebrahimi, S. Attarilar, C. Gode, S. R. Kandavalli, M. Shamsborhan, and Q. Wang, “Conceptual analysis on severe plastic deformation processes of shape memory alloys: mechanical properties and microstructure characterization,” Metals, vol. 13, no. 3, p. 447, 2023.
21. S. ur Rehman, M. Khan, A. N. Khan, M. I. Khan, L. Ali, and S. H. I. Jaffery, “Effect of precipitation hardening and thermomechanical training on microstructure and shape memory properties of Ti50Ni15Pd25Cu10 high temperature shape memory alloys,” J. Alloys Compd., vol. 616, pp. 275–283, 2014.

22. M. I. Khan, H. Y. Kim, T. Nam, and S. Miyazaki, "Formation of nanoscaled precipitates and their effects on the high-temperature shape-memory characteristics of a Ti50Ni15Pd25Cu10 alloy," Acta Mater., vol. 60, no. 16, pp. 5900–5913, 2012.

23. T. H. Nam, T. Saburi, and K. Shimizu, "Cu-content dependence of shape memory characteristics in Ti–Ni–Cu alloys," Mater. Trans. JIM, vol. 31, no. 11, pp. 959–967, 1990.

24. S. ur Rehman et al., "Transformation behavior and shape memory properties of Ti50Ni15Pd25Cu10 high temperature shape memory alloy at various aging temperatures," Mater. Sci. Eng. A, vol. 619, pp. 171–179, 2014.